ChemPubSoc Europe

DOI: 10.1002/cssc.201300651

Exposed Surfaces on Shape-Controlled Ceria Nanoparticles Revealed through AC-TEM and Water–Gas Shift Reactivity

Shilpa Agarwal,[b] Leon Lefferts,[b] Barbara L. Mojet,[b] D. A. J. Michel Ligthart,[c] Emiel J. M. Hensen,[c] David R. G. Mitchell,[d] Willem J. Erasmus,[d] Bruce G. Anderson,[d] Ezra J. Olivier,[e] Johannes H. Neethling,[e] and Abhaya K. Datye*[a]

Aberration-corrected transmission electron microscopy and high-angle annular dark field imaging was used to investigate the surface structures and internal defects of CeO_2 nanoparticles (octahedra, rods, and cubes). Further, their catalytic reactivity in the water–gas shift (WGS) reaction and the exposed surface sites by using FTIR spectroscopy were tested. Rods and octahedra expose stable (111) surfaces whereas cubes have primarily (100) facets. Rods also had internal voids and surface steps. The exposed planes are consistent with observed reactivity patterns, and the normalized WGS reactivity of octahedra and rods were similar, but the cubes were more reactive. In situ FTIR spectroscopy showed that rods and octahedra exhibit similar spectra for –OH groups and that carbonates and formates formed upon exposure to CO whereas for cubes clear differences were observed. These results provide definitive information on the nature of the exposed surfaces in these CeO_2 nanostructures and their influence on the WGS reactivity.

Introduction

Ceria (CeO_2) has been extensively investigated in the field of heterogeneous catalysis both as a catalyst and as a support for noble metals. This is due to its unique redox properties and high oxygen storage capacity (OSC), allowing it to quickly switch oxidation state between Ce^{4+} and Ce^{3+} in the stable fluorite structure.[1] Because of these redox properties, CeO_2 is used in a wide range of applications such as an ultraviolet (UV) absorber in sun blocks,[2] O_2 sensors,[3] and antioxidant in the field of biomedicine.[4] CeO_2 is commercially used as a catalyst support in applications such as three-way automotive exhaust catalysis (TWC)[5] and as solid electrolytes in low-temperature solid oxide fuel cells (SOFCs).[6] Further, the oxidation of CO,[7] NO,[8] hydrocarbons,[9] the low temperature water gas shift reaction (WGS),[10] and steam reforming of bio-oil[11] have been investigated on CeO_2 and CeO_2-supported catalysts.

In recent years, many studies have reported improved activity of CeO_2 catalysts through synthesis of CeO_2 nanostructures with controlled morphology.[12] The controlled morphology generates well-defined exposed crystallographic planes, which may lead to improved catalytic activity. Synthesis procedures for these CeO_2 nanocrystals are well developed for generating morphologies such as cubes,[13] rods,[1,7b,12a,13,14] wires,[1] tubes,[15] octahedra,[16] spindles,[17] 3D flower-like shapes,[18] and spheres.[14] These materials have also been studied in catalytic reactions. The literature shows that CeO_2 morphology can play an important role in catalytic performance.[1,7c,12a,14,15b,18] For instance, CeO_2 cubes were reported to exhibit excellent reducibility and high oxygen storage capacity (OSC) attributed to the presence of (100) planes.[19] CeO_2 rods attracted attention because they provide a high surface area. The rods are thought to expose (100) and (110) surfaces, which are less stable and thus more reactive than the (111) surface.[20] It has also been suggested that the CeO_2 rods have surface defects[7a,21] such as vacancy clusters, pits, and a high degree of surface roughness. CeO_2 rods have been reported to exhibit enhanced reactivity for the oxidation of CO,[1,7b,c] NO,[8] 1,2-dicholorethane, and ethyl acetate.[22]

The morphology of CeO_2 rods was deduced in the work of Zhou[7b] and Mai,[13] and the synthesis approach reported by

[a] Prof. A. K. Datye
Department of Chemical & Nuclear Engineering and
Center for Micro-Engineered Materials
University of New Mexico
Albuquerque, NM, 87109 (USA)
Fax: (+1) 505-277-1024
E-mail: datye@unm.edu

[b] S. Agarwal, Prof. L. Lefferts, Dr. B. L. Mojet
Catalytic Processes and Materials, MESA+Institute for Nanotechnology
Faculty of Science and Technology
University of Twente
PO Box 217, 7500 AE Enschede (The Netherlands)

[c] Dr. D. A. J. M. Ligthart, Prof. E. J. M. Hensen
Schuit Institute of Catalysis, Laboratory of Inorganic Materials Chemistry
Department of Chemical Engineering and Chemistry
Eindhoven University of Technology
PO Box 513, 5600 MB Eindhoven (The Netherlands)

[d] Dr. D. R. G. Mitchell, W. J. Erasmus, Dr. B. G. Anderson
Sasol Technology (Pty) Ltd.
PO Box 1, Sasolburg, 1947 (South Africa)

[e] Dr. E. J. Olivier, Prof. J. H. Neethling
Center for High Resolution Transmission Electron Microscopy
Nelson Mandela Metropolitan University
Port Elizabeth, 6031 (South Africa)

Supporting Information for this article is available on the WWW under http://dx.doi.org/10.1002/cssc.201300651.

Part of a Special Issue on "Shaping Nanostructures for Applications in Energy Conversion and Storage". To view the complete issue, visit: http://onlinelibrary.wiley.com/doi/10.1002/cssc.v6.10/issuetoc

these authors has become the standard recipe for the preparation of CeO_2 rods and cubes.[7c,21–23] Most recent studies rely on the morphology proposed in these early papers, suggesting that CeO_2 rods have exposed (100) and (110) surfaces and grow along the [110] direction.[23b,24] However, careful examination of the early studies shows that the limited resolution of TEM in those days made it difficult to obtain clear images of the surface regions. Furthermore, high-angle annular dark field (HAADF) imaging was not used in these studies to provide definitive shape information. More recently, it was suggested that CeO_2 rods can also expose (111) surfaces and it was implied that the origin of the enhanced reactivity for CO oxidation may not be connected with the surface facets but rather with the defects seen in these rods, particularly vacancy structures.[7a,8,17,25] Likewise, Asahina et al.[26] suggested that CeO_2 cubes exhibiting (100) surfaces may actually be composed of octahedral units, implying thereby that their surfaces are composed of (111) facets. In light of these uncertainties, we decided to investigate the surfaces of CeO_2 by using a combination of TEM technique as well as surface reactivity measurements.

Previous researchers used high-resolution TEM (HRTEM) to identify surface features and the morphology of the nanoparticles. Conventional HRTEM does not allow us to visualize the surfaces very clearly due to image delocalization and Fresnel fringes. The development of aberration-corrected transmission electron microscopy (AC-TEM) has pushed the resolution below 1 Å, both in TEM and STEM modes.[27] AC-TEM has recently been used to investigate the beam-induced cationic mobility on the surface of CeO_2 nanoparticles.[28] In the present study, we used a double aberration-corrected microscope (JEOL JEM-ARM 200F) equipped with both image and probe correctors. This combination of atomic-scale resolution in TEM and STEM images provides insights into the nature of the surfaces of these CeO_2 nanoshapes. As microscopy is a local technique, we have also included XRD and Brunauer–Emmett–Teller (BET) surface area measurements to provide a better average of the structure and morphology of these powders. To characterize the surface reactivity, we have used the water–gas shift (WGS) reaction as a probe reaction. In addition, FTIR spectroscopy of adsorbed CO allows us to obtain mechanistic insight into the surface reactions taking place on the respective CeO_2 nanoshapes. This combination of techniques allows us to present a complete picture of the nature of the surfaces in shape-controlled CeO_2 nanoparticles.

Results and Discussion

CeO_2 rods and cubes were synthesized by using the approach described by Mai et al.[13] The BET surface areas of ceria rods, octahedra, and cubes were found to be 80, 58, and 10 $m^2 g^{-1}$, respectively. The samples did not possess microporosity and have average pore sizes larger than 10 nm. The pore volumes of CeO_2 rods, octahedra, and cubes were 0.33, 0.20, and 0.05 $cm^3 g^{-1}$, respectively. The surface area is consistent with the particle sizes observed by SEM and TEM, showing that on average the cubes are significantly larger in size than the other two samples. Figure 1 shows the XRD patterns of the three

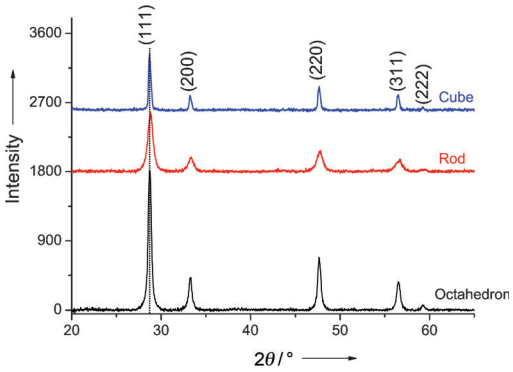

Figure 1. XRD patterns for controlled-morphology CeO_2 powders used in this study. The (111) reflection is highlighted with a vertical line and shows that the rods and octahedron samples have very similar lattice constants. The Supporting Information (Figure S1) presents an expanded view of the (311) reflection of these samples, showing the asymmetry in peak shape (related to bimodal particle size distribution) more clearly.

samples. The prominent CeO_2 diffraction peaks are consistent with the expected CeO_2 reflections according to ICDD card 43-1002.[29] The XRD peaks are broad due to the small size of the CeO_2 crystallites. Although it is difficult to derive average crystallite dimensions from Scherrer analysis for particle shapes that differ from spherical geometry, we have performed this analysis to obtain corroboration of our TEM observations. The sizes derived from the analysis of XRD data were as follows: Rods 29 nm, cubes 58.7 nm, and octahedra 51.2 nm. Our XRD data for CeO_2 nanoshapes are in agreement with the work of Mai et al.[13] (recipe we used for synthesis) as well as with the work of Wu et al. (2010),[21] Dai et al. (2012),[22] Gamarra et al. (2013),[30] Torrente-Murciano et al. (2013),[31] and Désaunay et al. (2013).[32]

All three samples in Figure 1 show some degree of asymmetry in the peak profile, as seen from the presence of a shoulder, or second peak on the left of the (311) reflection (see the Supporting Information, Figure S1; most prominent for rods).

We assign this shoulder to the existence of a bimodal particle size distribution, with the smaller particles showing a lattice constant that is larger than bulk CeO_2. The lattice expansion can be caused by the presence of Ce^{3+} ions in this ionic lattice as explained by the model presented by Tsunekawa et al.[33] A bimodal particle size distribution can be clearly observed in the SEM and TEM images and, hence, is consistent with this interpretation. In this sample set, all samples exhibit this bimodal particle size distribution, but we will show below that the particle size does not affect the surface termination of the CeO_2 nanoshapes. To establish the surface structure and morphology, the CeO_2 nanoshapes were analyzed by SEM, AC-TEM, and AC-STEM, the latter in bright field (BF) as well as in dark field (HAADF) imaging modes. We also embedded the rods in epoxy and prepared cross-section samples using an ultramicrotome, which allows us to analyze rods end-on. We next describe the morphology of these samples, followed by the catalytic reactivity and the FTIR spectroscopy of adsorbed species on the surface.

Octahedra

Figure 2 shows an SEM image of CeO_2 octahedra. Well-defined, faceted octahedra can be clearly seen. In addition, some fine-grained material is observed of which morphology cannot be determined at this magnification. As we show in the images to follow and in the Supporting Information (Figures S2 and S3), the fine-grained material has a similar morphology and exposed facets as the larger particles and the octahedral shape is the dominant one in this sample.

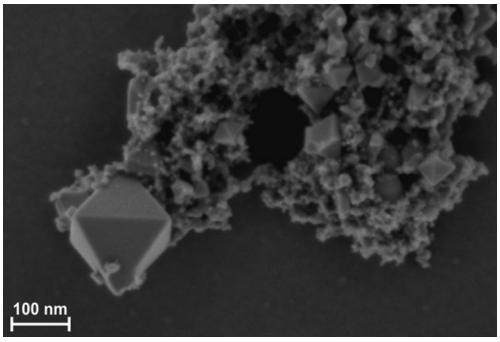

Figure 2. HRSEM image of the octahedra. Well-defined, faceted octahedra of differing size are present in this sample. This sample shows a distinct bimodal size distribution, with numerous particles that are much smaller than the large octahedra imaged here. This bimodal size distribution gives rise to the asymmetric peaks for the (311) reflection seen in Figure S1 in the Supporting Information.

BF and HAADF STEM images are shown in Figure 3. The BF image contrast can arise due to diffraction effects, for which the orientation of each particle also matters, whereas the HAADF image is dominated by atomic number and sample thickness. As we are only dealing with CeO_2, the differences in contrast in the HAADF images can be directly related to sample thickness and this allows for confirmation of the sample morphology. As shown in the inset, the octahedron is composed of eight {111} surfaces with the top and bottom oriented along the [100] direction. As seen in the dark field image, the prominent diamond-shaped particles are thicker in the center than at the edges; hence, they are consistent with an octahedron imaged edge-on. In addition to the dominant {111} planes, we also observe that the truncated ends of the octahedra have exposed {100} planes, as shown previously.[16,34] Finally, the octahedra have four sharp corners in the plane of square symmetry, directed in the $<110>$ directions. As illustrated in the model shown in the inset in Figure 3 and S3 in the Supporting Information, we see sharp corners where a {110} surface should have been present. The fact that we did not see any {110} surface facets and the fact that growth occurs along [110] direction indicates that the {110} surfaces are not stable.

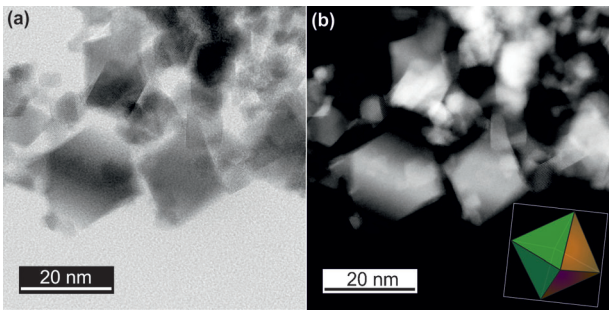

Figure 3. (a) BF and (b) HAADF STEM images showing the octahedral shapes. The thickness variation leads to the observed contrast change in the HAADF image (right), confirming the octahedral shape, as the center is thicker compared to the top and bottom (as seen from the inset). The smaller particles also expose the same dominant (111) surface, which is seen more clearly in the higher magnification images shown in Figures 3 and 4 and Figures S2 and S3 in the supporting information.

A higher magnification STEM image is shown in Figure 4. As the beam diameter is about 0.8 Å in this microscope, we can easily resolve the CeO_2 crystal lattice. The BF image is analogous to an HRTEM image; hence, contrast at these high magnifications comes from phase contrast. On the other hand, the HAADF image arises from incoherent scattering at high angles and is dominated by atomic number contrast. The bright lines consequently represent rows of Ce atoms, because O atoms will be almost invisible due to their low atomic number. The complementary BF and HAADF images allow us to see clearly the morphology of the sample and the nature of the surfaces. The particles are randomly oriented; hence, they are not lined up along the low-index zone axes, which is why most of them do not show cross fringes. Figure 4 shows that the CeO_2 {111} surfaces are smooth and free from any surface steps, defects, or surface reconstruction. A TEM image is a projection of a three-dimensional object. When the particle is large, some degree of surface roughness can arise because the surface is not perfect over large distances. The nature of the surfaces is further confirmed by the AC-TEM images (see Figure 5), where a large and a small octahedron are shown. The prominent {111} facets show clearly resolved rows of Ce-atom columns with small {100} facets. The inset is a model of the CeO_2 lattice showing that the AC-TEM image clearly resolves single-atom columns of Ce. Approximately 20–25 images were systematically analyzed for exposed crystal planes. Care was taken to ensure that selected regions did not contain multiple overlapping particles to avoid interference when analyzing the data. Additional images are shown in the Supporting Information (Figures S2 and S3), showing that even the smallest particles expose {111} facets.

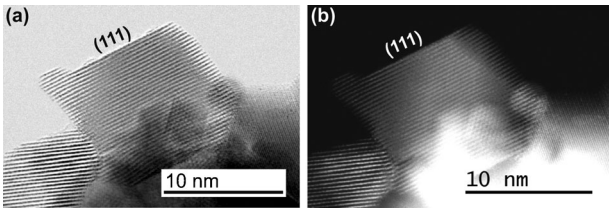

Figure 4. Higher magnification (a) BF and (b) HAADF STEM images showing the nature of the (111) surface. There is no signficant surface roughness evident on these.

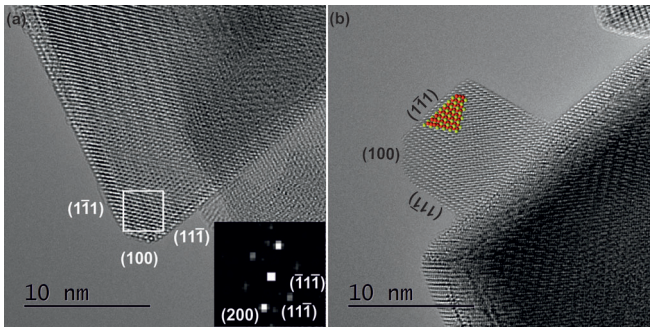

Figure 5. Aberration-corrected TEM images of large (a) and small (b) CeO_2 octahedra. These expose the (111) facets and very small (100) facets. The surface termination is abrupt, and there is no amorphous layer or surface roughness present. The inset in (b) shows the structure of the CeO_2 lattice (Ce atoms: green; O atoms: red) and the agreement between the white dots and the Ce atom columns.

Rods

Figure 6 shows a SEM image of the rods. This low magnification view reveals that the sample contains a uniform distribution of rods with a width of 5–10 nm and a length of about 200 nm, that is, an aspect ratio exceeding 20. The low-magnification view does not show the cross section of this rod, but it

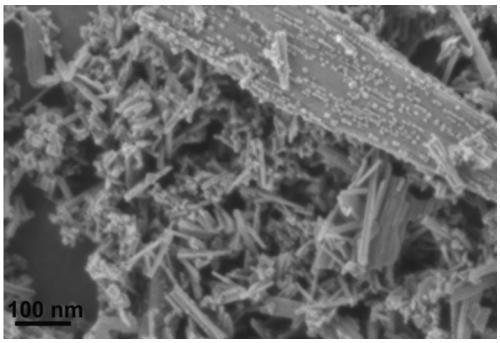

Figure 6. HRSEM image of the nanorods. These rods have a high aspect ratio length/width exceeding 20.

is clear that the primary exposed surface is along the length of the rods and that the ends contribute minimally to the total surface area. In Figure 7, we show BF and HAADF STEM images from these rods. The insets show fast Fourier transforms (FFTs) that provide information on the periodicities seen in the image. Based on the calibration of the microscope, we can index these spots as {111} planes, implying that the rods expose their {111} surfaces. The BF images also show characteristic regions of low contrast that appear to follow the crystallographic directions. The fact that these regions are dark in the HAADF image indicates less mass in those regions. These features could arise from voids within the structure or from surface steps. Recently, Florea et al., based on electron tomography, have assigned these low-contrast features to internal pores in the CeO_2 rods.[35] As can be seen in Figure 7a, surface steps are observed along the length of the rods. Therefore, we

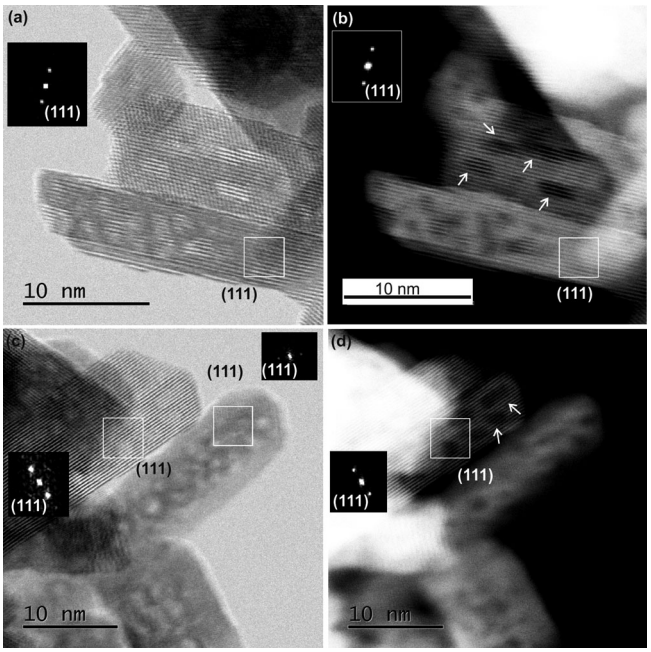

Figure 7. STEM images of CeO_2 rods. (a,c) BF images, (b,d) HAADF images. The inset in the figures is the FFT that allows indexing of the lattice planes. The rods expose (111) surfaces and have surface steps along the length. Areas of light contrast can be seen in the BF image and these same areas look dark in the HAADF image. The HAADF images confirm that these low-contrast features are voids in the CeO_2 rods that are bounded by (111) surfaces. The contrast variation in the HAADF image suggests a rectangular profile in the cross section.

conclude that these low-contrast features represent voids as well as surface steps in the CeO_2 rods. The shapes of these voids follow the stable surfaces of the CeO_2 structure; hence, these voids are bounded by {111} surfaces.

The CeO_2 rods grow along the [110] direction. This is confirmed by the lattice fringe images seen in Figure 8c, where we see (220) lattice fringes. We recorded numerous other images that confirm the growth direction to be [110]; this is consistent with the crystallography proposed in the literature by Mai et al.[13] and Zhou et al.[7b] These authors have further proposed a rectangular cross section for the rods that would expose (110) and (100) surfaces. However, as can be seen in Figures 7 and 8, our results show only {111} surfaces exposed by rods prepared according to Mai's recipe. In all of the images we analyzed, we did not observe a well-defined {110} facet in any of the rods we imaged. To visualize the top and bottom surfaces of these rods, we prepared a cross-section sample by embedding the rods in epoxy and using a microtome to prepare a cross section. Figure S4 shows the microtomed section where the rods are now embedded in epoxy. We reasoned that some of the rods must lie end-on so we could image their cross sections. Based on their aspect ratio (>20), any features with significantly smaller aspect ratios must represent rods. Because the rods are long, we could not achieve lattice resolution in the end-on views becaue the samples become too thick. We note that there are other proposed models for CeO_2 rods based on multiply twinned structures;[36]

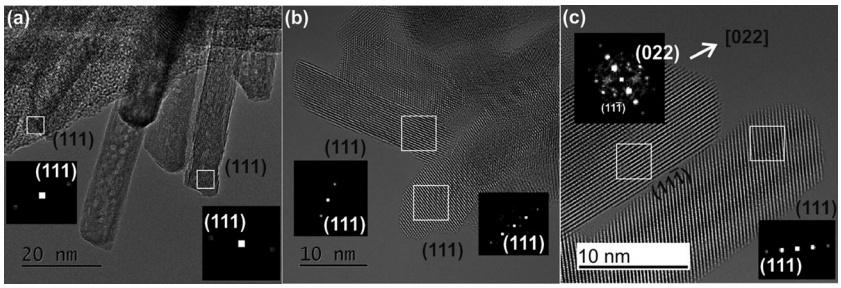

Figure 8. AC-TEM images of CeO_2 rods at two different magnifications [(a) and (b)]. Insets in the figures are FFTs of the boxed region in the images. (c) The lattice fringes confirm that the surfaces are {111} and the growth direction is $<110>$. The other images likewise show only {111} surface facets.

however, because the rods all show contiguous lattice fringes along their length, they cannot be composed of internally twinned units. We also do not observere the diamond-shaped cross sections suggested by Ta et al.[25] because the thickness variation seen in our HAADF images does not agree with such a cross section. Based on our results, we can state that the only prominent well-defined facet visible is the {111} surface, with the other surfaces being irregular and not well defined.

Cubes

Figure 9 shows a SEM image of the cubes. Well-defined cubic crystals range in size from 10–100 nm. The image also shows many smaller cubes giving rise to a bimodal particle size distribution, which may explain the the asymmetric peaks seen in the XRD pattern (see Figure S1). Figure 10 shows an image of a cube oriented along the cube edge. It is composed of {100} surfaces, but the corner at which a (110) surface would be expected is not well defined. We have included insets showing the atomic arrangement of the CeO_2 structure indicating that the (100) surface is not corrugated but perfectly matches what would be expected from a row of Ce atoms. Because the (100) surface is polar, the charge imbalance can be compensated by incomplete surface termination. As a result, we see incompletely occupied rows of Ce atoms at the surface instead of a fully occupied row of atoms as seen on the {111} surfaces.

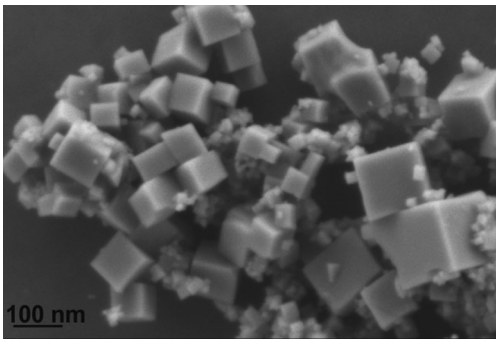

Figure 9. HRSEM image of cubes.

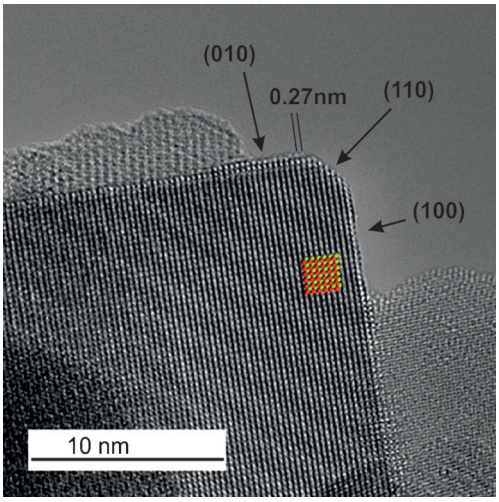

Figure 10. AC-TEM image of a cube nearly oriented along its cube axis [010]. The (100) surfaces can be clearly seen. They show single-atoms steps but no other form of surface reconstruction [i.e., into (111) facets]. The (110) surface is indicated at the cube corner, but it does not appear to be a well-defined facet. The structure of CeO_2 along the [010] direction is also included as an inset, to show the agreement with the white atom contrast on the right side of the image. The higher magnification view shows the arrangement of Ce (green) and O atoms (red).

WGS reactivity measurements

To investigate the catalytic behavior, the samples were tested in the WGS reaction. CeO_2 is known to be an excellent support for noble metals for this reaction.[10b] However, there are no reports of WGS reactivity on shape-controlled CeO_2 nanoparticles without added precious metals. Researchers in the past have tested these CeO_2 shapes for the CO/NO oxidation reaction, which are known to be influenced by the OSC and defects in the CeO_2 surfaces.[7a,8,21] The literature suggests that WGS involves active hydroxyl species (–OH) on the CeO_2 surface.[37] We have previously reported that the interaction of –OH species with CO depends on the specific CeO_2 nanoshapes.[23a] For this reason, WGS was chosen as a suitable probe reaction for evaluating the role of the CeO_2 surface on catalytic activity.

WGS catalytic measurements performed at 350 °C after hydrogen pre-treatment (see the Experimental Section for pretreatment details) are shown in Figure 11. The activity of the samples was expressed in mol CO per m^2 of CeO_2 to be able to correlate the surface structure with activity. The BET surface areas of CeO_2 rods, octahedra, and cubes were 80, 58, and 10 $m^2 g^{-1}$, respectively. Strikingly, the specific CO conversion rates for octahedra and rods are identical, whereas cubes are twice more active per surface area at 350 °C. For cubes, a slight deactivation in the first half hour was observed, but otherwise

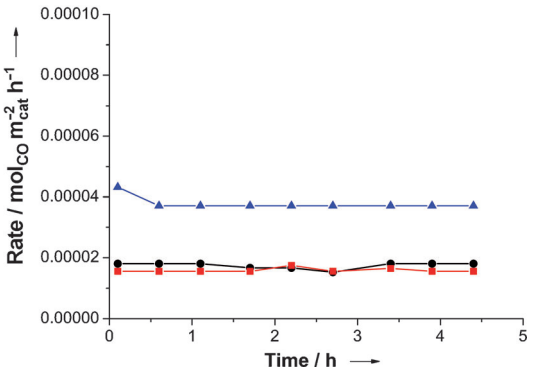

Figure 11. Rate of CO conversion per m^2 during WGS reaction for rods (red), octahedra (black), and cubes (blue) at 350 °C after H_2 pre-treatment at 500 °C.

all three samples show stable conversion over several hours. The CeO_2 nanoshapes preserved their shapes during reaction, as evident from TEM images of samples after reaction (see the Supporting Information, Figure S5).

The activity trends are consistent with our observations from AC-TEM on the exposed surfaces of the three CeO_2 shapes. The similar specific catalytic activities for rods and octahedra can be explained by the dominance of exposed {111} surfaces. The higher catalytic activity, generally expressed as CO conversion per gram of catalyst, of rods reported in the literature[1,7b,c] thus may be caused by the high surface area rather than the type of exposed crystal planes. On the other hand, CeO_2 cubes expose the highly active {100} surfaces, which clearly show enhanced specific WGS activity compared to the stable {111} surfaces. It should be recognized that the surface reactivity is not only determined by the exposed planes but also by the subsurface structure and the nature of defects. These features may also determine reducibility, oxygen-vacancy formation and catalytic activity. The WGS mechanism over CeO_2 nanoshapes and the nature of the reactive surface intermediates is currently under investigation and will be reported in the future.

FTIR spectroscopy

To characterize the chemistry of the exposed planes of the reduced CeO_2 nanoshapes in more detail, Fourier transform infrared spectroscopy (FTIR) at 350 °C was performed. The experimental conditions chosen for FTIR were the same as for WGS to gain spectroscopic insight related to the interaction of CeO_2 surfaces with CO/H_2O molecules during WGS catalytic reaction. The spectra have not been normalized to the surface area because the observed intensity was not only caused by the amount of species present but also by the light scattering properties of these nanoshapes, which are both size and shape dependent.[38]

After H_2 reduction, in flowing helium at 350 °C

Transmission FTIR data of the H_2-reduced (for details see the Experimental Section) CeO_2 nanoshapes in a helium flow at 350 °C are displayed in Figure 12 (black lines). Figure 12 a–c shows the range of O–H stretch vibrations between 3800–3000 cm^{-1}. The three nanoshapes show distinct –OH stretching bands, with different intensities depending on the specific shape.

The hydroxyl stretch regions for octahedra and rods look quite similar, showing a strong band at 3639 cm^{-1} for bridging hydroxyls, with a shoulder at 3669 cm^{-1} arising from single-coordinated hydroxyl species.[39] In addition, both samples show multi-bonded and hydrogen bonded –OH species between 3600 and 3000 cm^{-1}.[33a] CeO_2 rods have a significant higher intensity for the multi-bonded hydroxyl species at 3454 cm^{-1} than octahedra. The higher amount of bridging –OH groups for rods is most likely attributable to the voids and surface roughness observed with AC-TEM (Figures 7 and 8).

The hydroxyl region for cubes (Figure 12 c) looks more complex than those for octahedra and rods. Closer examination reveals that cubes have the same –OH bands as rods but with different relative intensities. In addition, three additional pronounced hydroxyl bands at 3738, 3602, and 3253 cm^{-1} are observed for cubes.

So far, these specific hydroxyl bands have not been individually assigned in the literature. The different surface termination for CeO_2 {111} and CeO_2 {100} most likely explains why cubes show specific hydroxyl bands more strongly than rods and octahedra. The CeO_2 (111) surface has both Ce and O exposed in the top layer, whereas CeO_2 (100) is either O terminated or Ce terminated (see the Supporting Information, Figure S6). These different surface terminations will lead to hydroxyl groups with different stretching frequency. Thus, the FTIR spectra show that rods and octahedra resemble each other in surface termination, as evidenced by the hydroxyl vibration bands, whereas cubes clearly have a different distribution of the surface –OH groups.

Figure 12 d–f (black lines) show the stretching and deformation bands of carbonates (1800–800 cm^{-1}) for octahedra, rods, and cubes.[40] These carbonate species were formed on the fresh CeO_2 samples due to interaction with atmospheric CO_2 when exposed to air.[23a,39a] Clearly, these carbonates are stable towards the reduction treatment in hydrogen. In comparison to our previous work on fresh CeO_2 samples at 200 °C, reduced CeO_2 nanoshapes are cleaner due to the decomposition of some additional carbonates during hydrogen pretreatment at higher temperatures.[23a]Although the bands look similar for the three samples, cubes clearly exhibit sharper carbonate bands at slightly different positions (maxima at 1392 and 1456 cm^{-1}) than octahedra and rods (1370 and 1456 cm^{-1}).

CO adsorption at 350 °C

After 30 min in helium flow at 350 °C, the CeO_2 nanoshapes were exposed to CO and the FTIR spectra after 30 min in CO are shown in Figure 12 (red lines). Only subtle changes are observed in the –OH region upon exposure to CO (Figure 12 a–c). For octahedra and rods, the broad band related to multi-coordinated and hydrogen-bonded hydroxyls decreased in intensity. For rods, a slight and increased intensity for bridged –OH

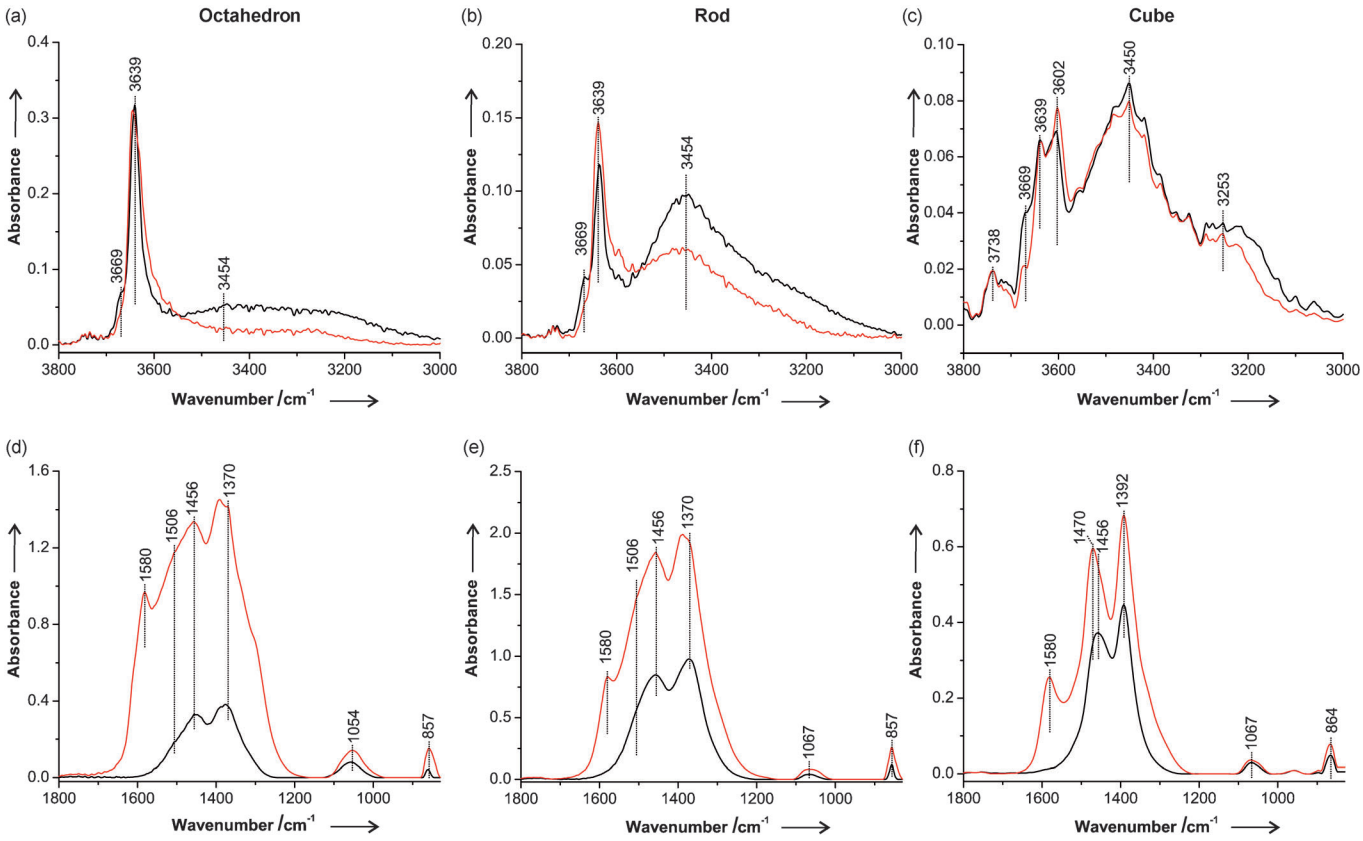

Figure 12. Baseline-corrected in situ FTIR spectra at 350 °C of H_2-reduced CeO_2 rods, octahedra, and cubes in He flow (black spectrum) followed by 33 vol% CO/He (red spectrum) from (a)–(c) 3800–3000 cm^{-1} (hydroxyl region) and (d)–(f) 1800–800 cm^{-1} (carbonates and formates region).

groups (3639 cm^{-1}) can be seen. For cubes, a minor decrease in the hydrogen-bonded hydroxyl groups (3253 cm^{-1}) was found. All three nanoshapes show a significant decrease in intensity for single-coordinated –OH groups at 3669 cm^{-1}.

The interaction of CO with –OH groups leads to the formation of adsorbed formate species as evidenced by the band at 1580 cm^{-1} in Figure 12d–f and C–H stretching bands at 2846 and 2932 cm^{-1} (Figure S7).[10c,41] In addition to formates, carbonates are formed upon exposure of the nanoshapes to CO (Figure 12d–f). The spectral fingerprint for the carbonates after exposure to CO is very similar for octahedra and rods, with multiple bands between 1600 and 1200 cm^{-1}. For CeO_2 cubes, the two bands initially present increased in intensity. CO adsorption on fresh CeO_2 shapes at 200 °C followed a similar trend, although exact band positions and shapes were different.[23a] The formate and carbonate bands on cubes are relatively narrow compared to the formate and carbonate on octahedra and rods. This suggests, in combination with the well-resolved –OH vibrations, that the surface adsorption sites on cubes are more distinct than on the other two shapes.

The AC-TEM results in this study show that rods and octahedra expose {111} surface planes that result in similar catalytic WGS activities per m^2. In addition, the type of hydroxyl species present and the surface interaction with CO on octahedra and rods are similar, which is consistent with the identical WGS activities per m^2 (Figure 11). Cubes consist of the more reactive {100} surface planes, which have different –OH bands and interactions with CO, resulting in a higher WGS reactivity per m^2.

Conclusions

We used aberration-corrected TEM and HAADF STEM to investigate the morphology of shape-controlled CeO_2 nanoparticles. Although differently shaped CeO_2 particles were generated, we found that the WGS activity normalized per m^2 was identical for CeO_2 octahedra and rods, whereas CeO_2 cubes were much more reactive. Likewise, FTIR data of adsorbed CO and OH groups show a similar surface structure and reactivity for rods and octahedra, which were again different from the cubes. A detailed investigation of the CeO_2 nanoparticles was conducted by AC-TEM and AC-STEM. The exposed surfaces were identified, and the nature of the surfaces examined at atomic resolution. The TEM observations help us explain the reactivity trends, as we found that both CeO_2 octahedra and rods expose {111} surfaces. On the other hand, the CeO_2 cubes expose {100} surfaces, which are consistent with their cubic habits. The combination of WGS reactivity and FTIR and TEM measurements help us to reveal the true nature of the exposed surfaces in these CeO_2 nanoparticles.

Experimental Section

Catalyst preparation

All materials used were of analytical purity, obtained from Sigma–Aldrich. CeO_2 rods and cubes were synthesized through the hydrothermal procedure first reported by Mai.[13] $Ce(NO_3)_3{\cdot}6H_2O$ (2.17 g) and NaOH (24 g) were dissolved in 5 and 35 mL deionized water, respectively. The solutions were mixed and stirred for 30 min. This resulted in the formation of milky slurry, which was then transferred to an autoclave (125 mL) and filled with deionized water up to 80% of the total volume of the autoclave. The solution was subjected to hydrothermal treatment for 24 h at temperatures of 100 (for rods) and 180 °C (for cubes). Next, the fresh precipitates (yellow color for rods and white for cubes) were separated by centrifugation, washed with deionized water several times, followed by washing in ethanol and drying at 60 °C in air overnight. The reference shape used in this study was the CeO_2 octahedron (99.9% pure), which was obtained from Sigma–Aldrich and had an average particle size smaller than 25 nm. The samples were calcined at 500 °C (heating rate 5 K min^{-1}) for 4 h in synthetic air (flow rate = 50 mL min^{-1}) and subsequently cooled down to room temperature in air before use.

HRSEM, TEM, BET, and XRD characterization

The HRSEM and TEM images (after WGS testing) of the CeO_2 nanoshapes were recorded by using Carl Zeiss Merlin and GATAN CM300ST-FEG electron microscope (operated at an acceleration voltage of 300 kV), respectively. BET surface areas were determined by performing N_2 physisorption using a Micromeritics Tristar instrument. The samples were out-gassed in vacuum at 300 °C for 24 h prior to analysis.

X-Ray diffraction data were recorded with a Bruker D2 Phaser diffractometer using CuK_α radiation ($\lambda = 0.1544$ nm). XRD patterns were measured in reflection geometry in the 2θ range between 0° and 90°.

AC-TEM and STEM measurements

The investigation was performed by using a double-aberration-corrected JEOL ARM200F operated at 200 kV accelerating voltage equipped with a Gatan GIF Quantum with dual EELS capability as well as an Oxford XMax 80 EDS (Energy-dispersive X-Ray spectroscopy) detector. The TEM imaging was conducted by using a Gatan Ultrascan USFTXP camera with the STEM imaging performed in both BF and ADF mode. The probe used for STEM imaging had a convergence angle of 17 mrad with a probe current density of approximately 68 pA. The acceptance-angle range used for ADF imaging was 68–230 mrad. The nominal probe diameter for STEM imaging was 0.08 nm, and the point resolution for TEM imaging was 0.11 nm. We used the Gatan Digital Micrograph software for analysis of the images and the CrystalMaker software for visualizing the structure of CeO_2 along different crystallographic projections.

FTIR spectroscopy

Transmission FTIR measurements were recorded with a Bruker Vector 22 by averaging 128 scans with a spectral resolution of 4 cm^{-1} and time intervals of 120 s. The background spectrum was recorded by using an empty cell. The FTIR signal was recorded with MCT (mercury–cadmium–telluride) detector. A self-supporting pellet of about 13–15 mg of sample was pressed and added into a homemade stainless-steel cell. The samples were pretreated in H_2 flow (20 mL min^{-1}) at 450 °C for 1 h (heating rate 5 °C min^{-1}). After pretreatment, the FTIR cell was cooled to 150 °C in a He flow and then heated to reaction temperature. He was dried by using a Varian Chromopack CP17971 gas clean moisture filter, to trap any moisture in the gases. For CO adsorption experiments, 33 vol% CO (Hoekloos 4.7) in He (Hoekloos 5.0, total flow 20 mL min^{-1}) was used. All tubes from the gas panel to the cell were preheated to 200 °C to avoid a sudden temperature drop in the FTIR cell.

Background: empty cell.

WGS catalytic activity testing

WGS catalytic activity measurements were performed in a parallel ten-flow microreactor system. For the H_2O/He stream, He was introduced into an evaporator mixer unit filled with deionized water, which was connected to a liquid flow controller and mass flow controller (Bronkhorst) to control the H_2O/He flow. All the tubes from the evaporator unit to the microreactor was heated above 100 °C to avoid condensation in the line. High-purity gases were used in the catalytic experiments [e.g., H_2, He (5.0) and CO (4.7, from Linde)]. The CO/H_2O reaction feed ratio used was 1:3 balanced by He, and the total volume flow rate was 200 mL min^{-1}, resulting in a gas hourly space velocity (GHSV) of about $2.4{\cdot}10^4$ mL $g_{cat.}^{-1}$ h^{-1}. The particle size of the samples was between 125–250 μm, and the amount of catalyst used was 50 mg diluted with 320 mg of SiC of the same sieve fraction. The reactions were performed at atmospheric pressure and at 350 °C. The catalyst was reduced in H_2 balanced by He flow (H_2/He = 1:4) at 500 °C for 1 h prior to catalytic measurements. After pretreatment, the reactor system was cooled to 150 °C in He flow and then heated to reaction temperature in a CO/H_2O/He flow. The effluent stream from the reactor was directed to a Compact GC (Interscience) equipped with Porapak Q (TCD—thermal conductivity detector) and Molecular sieve 5A (TCD) columns for online detection of H_2, CO, and CO_2 gases.

Acknowledgements

The electron microscopy was performed at the Center for High Resolution Transmission Electron Microscopy at the Nelson Mandela Metropolitan University and at the Sasol Technology in Sasolburg, South Africa. The National Research Foundation, Sasol, and the Department of Science and Technology in South Africa are acknowledged for financial support. Additional SEM work was performed at the University of New Mexico. The research was supported by DOE grant DE-FG02-05ER15712 and NSF grant OISE 0730277, Partnership for International Research and Education (PIRE). S.A. acknowledges the ADEM Innovation Lab for financial support (Project Number 30961318). Part of the work was performed under auspices of the Netherlands Institute for Catalysis Research (NIOK). The authors also gratefully acknowledge M. A. Smithers for HRSEM and TEM imaging and Karin Altena-Schildkamp for BET measurements performed at University of Twente. We would like to thank Ruben Lubkemann and Bert Geerdink for technical assistance.

Keywords: ceria · heterogeneous catalysis · nanoparticles · aberration-corrected TEM · water–gas shift reaction

[1] Tana, M. Zhang, J. Li, H. Li, Y. Li, W. Shen, *Catal. Today* **2009**, *148*, 179 – 183.
[2] J. F. D. Lima, R. F. Martins, C. R. Neri, O. A. Serra, *Appl. Surf. Sci.* **2009**, *255*, 9006 – 9009.
[3] a) N. Izu, W. Shin, N. Murayama, S. Kanzaki, *Sens. Actuators B* **2002**, *87*, 95 – 98; b) H. J. Beie, A. Gnorich, *Sens. Actuators B* **1991**, *4*, 393 – 399.
[4] A. S. Karakoti, N. A. Monteiro-Riviere, R. Aggarwal, J. P. Davis, R. J. Narayan, W. T. Self, J. McGinnis, S. Seal, *JOM* **2008**, *60*, 33 – 37.
[5] A. F. Diwell, R. R. Rajaram, H. A. Shaw, T. J. Truex in *Studies in Surface Science and Catalysis, Vol. 71* (Ed.: A. Crucq), Elsevier, Amsterdam, **1991**, pp. 139 – 152.
[6] a) C. Xia, M. Liu, *Solid State Ionics* **2002**, *152 – 153*, 423 – 430; b) B. C. H. Steele, *J. Power Sources* **1994**, *49*, 1 – 14.
[7] a) X. Liu, K. Zhou, L. Wang, B. Wang, Y. Li, *J. Am. Chem. Soc.* **2009**, *131*, 3140 – 3141; b) K. Zhou, X. Wang, X. Sun, Q. Peng, Y. Li, *J. Catal.* **2005**, *229*, 206 – 212; c) Z. Wu, M. Li, S. H. Overbury, *J. Catal.* **2012**, *285*, 61 – 73.
[8] L. Liu, Y. Cao, W. Sun, Z. Yao, B. Liu, F. Gao, L. Dong, *Catal. Today* **2011**, *175*, 48 – 54.
[9] A. Trovarelli, C. de Leitenburg, M. Boaro, G. Dolcetti, *Catal. Today* **1999**, *50*, 353 – 367.
[10] a) R. J. Gorte, S. Zhao, *Catal. Today* **2005**, *104*, 18 – 24; b) R. J. Gorte, *AIChE J.* **2010**, *56*, 1126 – 1135; c) G. Jacobs, P. Patterson, L. Williams, D. Sparks, B. Davis, *Catal. Lett.* **2004**, *96*, 97 – 105.
[11] S. Czernik, R. Evans, R. French, *Catal. Today* **2007**, *129*, 265 – 268.
[12] a) K. Zhou, Y. Li, *Angew. Chem.* **2012**, *124*, 622 – 635; *Angew. Chem. Int. Ed.* **2012**, *51*, 602 – 613; b) A. Tschope, W. Liu, M. Flytzani-Stephanopoulos, J. Y. Ying, *J. Catal.* **1995**, *157*, 42 – 50.
[13] H.-X. Mai, L.-D. Sun, Y.-W. Zhang, R. Si, W. Feng, H.-P. Zhang, H.-C. Liu, C.-H. Yan, *J. Phys. Chem. B* **2005**, *109*, 24380 – 24385.
[14] D. Zhang, X. Du, L. Shi, R. Gao, *Dalton Trans.* **2012**, *41*, 14455 – 14475.
[15] a) W.-Q. Han, L. Wu, Y. Zhu, *J. Am. Chem. Soc.* **2005**, *127*, 12814 – 12815; b) C. Sun, H. Li, L. Chen, *Energy Environ. Sci.* **2012**, *5*, 8475 – 8505.
[16] Z. L. Wang, X. Feng, *J. Phys. Chem. B* **2003**, *107*, 13563 – 13566.
[17] S. Wang, L. Zhao, W. Wang, Y. Zhao, G. Zhang, X. Ma, J. Gong, *Nanoscale* **2013**, *5*, 5582 – 5588.
[18] a) H. Li, G. Lu, Q. Dai, Y. Wang, Y. Guo, Y. Guo, *ACS Appl. Mater. Interfaces* **2010**, *2*, 838 – 846; b) L.-S. Zhong, J.-S. Hu, A.-M. Cao, Q. Liu, W.-G. Song, L.-J. Wan, *Chem. Mater.* **2007**, *19*, 1648 – 1655.
[19] Z. Yang, K. Zhou, X. Liu, Q. Tian, D. Lu, S. Yang, *Nanotechnology* **2007**, *18*, 185606.
[20] Z. Yang, T. K. Woo, M. Baudin, K. Hermansson, *J. Chem. Phys.* **2004**, *120*, 7741 – 7749.
[21] Z. Wu, M. Li, J. Howe, H. M. Meyer, S. H. Overbury, *Langmuir* **2010**, *26*, 16595 – 16606.
[22] Q. Dai, H. Huang, Y. Zhu, W. Deng, S. Bai, X. Wang, G. Lu, *Appl. Catal. B* **2012**, *117 – 118*, 360 – 368.
[23] a) S. Agarwal, L. Lefferts, B. L. Mojet, *ChemCatChem* **2013**, *5*, 479 – 489; b) R. Si, M. Flytzani-Stephanopoulos, *Angew. Chem.* **2008**, *120*, 2926 – 2929; *Angew. Chem. Int. Ed.* **2008**, *47*, 2884 – 2887; c) G. Yi, H. Yang, B. Li, H. Lin, K.-i. Tanaka, Y. Yuan, *Catal. Today* **2010**, *157*, 83 – 88; d) A. Ciftci, D. A. J. M. Ligthart, P. Pastorino, E. J. M. Hensen, *Appl. Catal. B* **2013**, *130 – 131*, 325 – 335; e) Y. Guan, D. A. J. M. Ligthart, Ö. Pirgon-Galin, J. A. Z. Pieterse, R. A. Santen, E. J. M. Hensen, *Top. Catal.* **2011**, *54*, 424 – 438.
[24] a) S. Chang, M. Li, Q. Hua, L. Zhang, Y. Ma, B. Ye, W. Huang, *J. Catal.* **2012**, *293*, 195 – 204; b) J. Han, H. J. Kim, S. Yoon, H. Lee, *J. Mol. Catal. A: Chem.* **2011**, *335*, 82 – 88; c) W.-Q. Han, W. Wen, J. C. Hanson, X. Teng, N. Marinkovic, J. A. Rodriguez, *J. Phys. Chem. C* **2009**, *113*, 21949 – 21955; d) G. Yi, Z. Xu, G. Guo, K.-i. Tanaka, Y. Yuan, *Chem. Phys. Lett.* **2009**, *479*, 128 – 132; e) N. Yi, R. Si, H. Saltsburg, M. Flytzani-Stephanopoulos, *Energy Environ. Sci.* **2010**, *3*, 831 – 837.
[25] N. Ta, J. Liu, S. Chenna, P. A. Crozier, Y. Li, A. Chen, W. Shen, *J. Am. Chem. Soc.* **2012**, *134*, 20585 – 20588.
[26] S. Asahina, S. Takami, T. Otsuka, T. Adschiri, O. Terasaki, *ChemCatChem* **2011**, *3*, 1038 – 1044.
[27] a) S. J. Pennycook, *Ultramicroscopy* **2012**, *123*, 28 – 37; b) O. L. Krivanek, M. F. Chisholm, M. F. Murfitt, N. Dellby, *Ultramicroscopy* **2012**, *123*, 90 – 98.
[28] a) U. M. Bhatta, I. M. Ross, T. X. T. Sayle, D. C. Sayle, S. C. Parker, D. Reid, S. Seal, A. Kumar, G. Möbus, *ACS Nano* **2012**, *6*, 421 – 430; b) G. Möbus, Z. Saghi, D. C. Sayle, U. M. Bhatta, A. Stringfellow, T. X. T. Sayle, *Adv. Funct. Mater.* **2011**, *21*, 1971 – 1976.
[29] JCPDS, Vol. PCPDFWIN v. 2.4, **2003**.
[30] D. Gamarra, A. L. Cámara, M. Monte, S. B. Rasmussen, L. E. Chinchilla, A. B. Hungría, G. Munuera, N. Gyorffy, Z. Schay, V. C. Corberán, J. C. Conesa, A. Martínez-Arias, *Appl. Catal. B* **2013**, *130 – 131*, 224 – 238.
[31] L. Torrente-Murciano, A. Gilbank, B. Puertolas, T. Garcia, B. Solsona, D. Chadwick, *Appl. Catal. B* **2013**, *132 – 133*, 116 – 122.
[32] T. Désaunay, G. Bonura, V. Chiodo, S. Freni, J. P. Couzinié, J. Bourgon, A. Ringuedé, F. Labat, C. Adamo, M. Cassir, *J. Catal.* **2013**, *297*, 193 – 201.
[33] S. Tsunekawa, K. Ishikawa, Z. Q. Li, Y. Kawazoe, A. Kasuya, *Phys. Rev. Lett.* **2000**, *85*, 3440 – 3443.
[34] J. P. Y. Tan, H. R. Tan, C. Boothroyd, Y. L. Foo, C. B. He, M. Lin, *J. Phys. Chem. C* **2011**, *115*, 3544 – 3551.
[35] I. Florea, C. Feral-Martin, J. Majimel, D. Ihiawakrim, C. Hirlimann, O. Ersen, *Cryst. Growth Des.* **2013**, *13*, 1110 – 1121.
[36] N. Bugayeva, *Mater. Res. Soc. Symp. Proc.* **2005**, *876*, 195 – 200.
[37] a) K. G. Azzam, I. V. Babich, K. Seshan, L. Lefferts, *J. Catal.* **2007**, *251*, 153 – 162; b) K. G. Azzam, I. V. Babich, K. Seshan, L. Lefferts, *J. Catal.* **2007**, *251*, 163 – 171; c) G. Jacobs, E. Chenu, P. M. Patterson, L. Williams, D. Sparks, G. Thomas, B. H. Davis, *Appl. Catal. A* **2004**, *258*, 203 – 214; d) T. Shido, Y. Iwasawa, *J. Catal.* **1992**, *136*, 493 – 503.
[38] P. Yang, H. Wei, H.-L. Huang, B. A. Baum, Y. X. Hu, G. W. Kattawar, M. I. Mishchenko, Q. Fu, *Appl. Opt.* **2005**, *44*, 5512 – 5523.
[39] a) C. Binet, M. Daturi, J.-C. Lavalley, *Catal. Today* **1999**, *50*, 207 – 225; b) A. Badri, C. Binet, J.-C. Lavalley, *J. Chem. Soc. Faraday Trans.* **1996**, *92*, 4669 – 4673.
[40] G. N. Vayssilov, M. Mihaylov, P. S. Petkov, K. I. Hadjiivanov, K. M. Neyman, *J. Phys. Chem. C* **2011**, *115*, 23435 – 23454.
[41] C. Binet, A. Jadi, J.-C. Lavalley, *J. Chim. Phys. Phys.-Chim. Biol.* **1992**, *89*, 1779 – 1797.

Received: July 5, 2013
Published online on September 24, 2013